Biomaterials Science

ROYAL SOCIETY OF CHEMISTRY

PAPER

View Article Online
View Journal | View Issue

Cite this: *Biomater. Sci.*, 2025, **13**, 6879

Cationic PPC liposomes with dual targeting modules for enhanced liver fibrosis therapy *via* the extracellular matrix barrier

Yong Li,†[a,c] Yuanyuan Zhou, †[b] Lifang Wu,†[b] Quanyuan Gao[b] and Wei Wang*[a]

Activation of hepatic stellate cells (HSCs) is a key driver of fibrogenesis, while perisinusoidal collagen I deposition establishes biophysical barriers that impede therapeutic delivery. To address this challenge, we developed a cationic liposome nanomicelle system (LIP/RSC) based on a polyenyl phosphatidylcholine (PPC) matrix, functionalized with collagenase I and dual silybin B-retinoic acid (silybin-RA) moieties. In this design, retinoic acid (RA) was covalently conjugated to two distinct components: (i) silybin B to form a targeted therapeutic complex (silybin-RA), and (ii) DSPE-PEG2000-NH_2 to construct a long-circulating carrier (RA-DSPE-PEG2000). The resulting system embodies an innovative HSC-ECM dual-targeting strategy through the integration of dual RA modification technology—combining silybin B-targeting modification with DSPE-PEG2000 long-circulation modification—and spatiotemporally controlled silybin B release. The LIP/RSC system exhibited cell-selective drug release profiles, with a 4-fold greater release of silybin B in CCl_4-activated HSCs (LX-2-CCl_4) than in hepatocytes (WRL68), accompanied by collagen normalization. The system conferred dual pharmacodynamics: slow-release kinetics-prolonged circulation time (≥72 h) while enabling receptor-mediated HSC targeting and collagenase I activity-enhanced fibrotic barrier penetration, resulting in a 2.1-fold increase in the silybin B release efficiency in 8–72 h post-injection and an 85% reduction in the total collagen content in fibrotic murine models. This study validates LIP/RSC as an integrated nanoplatform that synergizes matrix remodeling with targeted drug delivery, thereby demonstrating enhanced therapeutic efficacy against hepatic fibrosis.

Received 20th August 2025,
Accepted 13th October 2025

DOI: 10.1039/d5bm01262g

rsc.li/biomaterials-science

1. Introduction

Globally, hepatic disorders account for approximately two million deaths annually, with cirrhosis-associated complications accounting for 50% of this mortality. Cirrhosis is ranked among the top 20 contributors to disability-adjusted life years (DALYs) and years of life lost worldwide.[1,2] Chronic liver injury progresses through a sequential pathogenic cascade: initial fibrotic remodeling precedes irreversible cirrhotic transformation. This progression underscores the critical importance of early therapeutic intervention during reversible fibrotic stages.[3] Clinical evidence confirms that pharmacological intervention during early fibrosis stages can achieve disease regression.[4] Current strategies predominantly employ hepatoprotective agents (*e.g.*, silymarin and glycyrrhizic acid derivatives) that exert multimodal anti-fibrotic effects through anti-inflammatory activity, hepatocyte membrane stabilization, and oxidative stress mitigation.[5–7] Nevertheless, therapeutic efficacy remains constrained by pharmacological limitations, including poor aqueous solubility, inadequate tissue specificity, and suboptimal biodistribution profiles. These physicochemical challenges frequently result in diminished bioavailability and off-target effects, significantly compromising clinical outcomes.[8–10]

Liver fibrosis is a dynamic process characterized by the abnormal accumulation of extracellular matrix (ECM) fibers (*e.g.*, collagen), and the increased expression of α-smooth muscle actin (α-SMA) in activated HSCs.[11] Following liver injury, hepatic stellate cells located in the perisinusoidal space are activated from a quiescent state by reactive oxygen intermediates or cytokines, transforming into proliferative and fibrotic myofibroblasts.[11,12] The activation of HSCs plays a pivotal role in the development of liver fibrosis, making them the primary target cells for anti-fibrotic therapy.[13] In normal

[a]*Department of Hepatobiliary Surgery, Second Attached Hospital of Fujian Medical University, Quanzhou, Fujian 362018, China. E-mail: Wangwei9909@fjmu.edu.cn, xmdrlee@163.com*
[b]*Department of Pharmacy, Second Affiliated Hospital of Xiamen Medical College, Xiamen, Fujian 361023, China. E-mail: zhouyuanyuan@xmmc.edu.cn, 84621460@163.com*
[c]*Department of Hepatobiliary Surgery, Second Affiliated Hospital of Xiamen Medical College, Xiamen, Fujian 361023, China*
†These authors contributed equally to this work.

liver function, HSCs participate in RA storage, vascular regulation, ECM homeostasis, drug detoxification and immune tolerance through endothelial cell interactions[14] and may promote hepatocyte mitosis and quality maintenance by secreting hepatocyte growth factors.[15,16] Current antifibrotic strategies address both matrix accumulation and drug penetration barriers through mechanistically distinct yet synergistic approaches.[17–19]

Significantly, in preclinical studies, protease-modified nanocarriers have demonstrated enhanced fibrotic ECM penetration capacity, enabling effective anti-fibrotic therapy.[19,20] Similarly, lipid-based nano-formulations exhibit improved hepatic targeting and retention profiles, showing promise against liver inflammation,[21,22] fibrosis,[23] and hepatocellular carcinoma in animal models.[24,25] However, the clinical translation of these systems faces two interconnected bottlenecks: the dense collagen-rich ECM physically blocking nanocarrier infiltration into activated HSCs, combined with insufficient targeting specificity to direct therapeutics exclusively to HSCs. In addition, studies have shown that silybin can reduce the activation and proliferation of HSCs *in vitro* and in culture[26,27] and decrease collagen accumulation in experimental rat liver fibrosis models.[19,28–30,31] However, silymarin exhibits a very short metabolic half-life and limited residence time in the liver, which necessitates increasing the dose and frequency of administration.[32] We hypothesized that enzymatically degrading fibrotic barriers while actively targeting HSCs would synergistically enhance the bioavailability of silybin B, leading to unprecedented fibrotic resolution.

Our integrated targeting strategy combines two complementary components: (i) covalent conjugation of silybin B with RA[33,34] generates a dual-function agent (silybin-RA) with HSC-targeting and membrane-anchoring capabilities; and (ii) silybin-RA-grafted DSPE-PEG2000 forms long-circulating carriers that maintain targeting specificity through PEG-mediated steric stabilization. Subsequently, we engineered a cationic liposomal–micellar hybrid system using polyenyl phosphatidylcholine (PPC) as a structural matrix, which was co-functionalized with collagenase I and silybin-RA (LIP/RSC). In fibrotic hepatic tissue, collagenase I modification of LIP/RSC enables enzymatic degradation of collagen-rich ECM barriers, while the RA-DSPE-PEG2000 component extends systemic circulation through steric stabilization effects.[35] Furthermore, RA modification allows LIP/RSC to efficiently recognize and target HSCs. Unlike passive targeting *via* the enhanced permeability and retention (EPR) effect[36] or non-specific receptor-mediated uptake,[37] RA modification enables ligand–receptor recognition specific to activated HSCs, which overexpress retinoic acid receptors (RARα/γ) during fibrogenesis.[38,39]

Herein, we propose a matrix-cellular dual-targeting paradigm through the rational integration of collagenase-mediated ECM remodeling and RA-directed HSC homing. The PPC matrix enhances the solubility of silybin-RA, synergizing with collagenase I-mediated enzymatic degradation of fibrotic ECM components to overcome spatial drug delivery barriers. Surface-engineered silybin B further enabled precise targeting of HSCs (Fig. 1). For comparison, silybin liposomal micelles (LIP/S), RA-modified liposomal micelles (LIP/R) and silybin-RA-modified liposomal micelles (LIP/RS) were also prepared as controls (Fig. 1a). The uptake efficiency of HSCs (LX-2) was comparatively evaluated under type I collagen (Col I)-overloaded conditions. Subsequent in-depth investigation of their *in vivo* delivery characteristics was conducted in a hepatic fibrosis model, with macro-level organ distribution profiling localization analysis. Comprehensive multi-dimensional functional characterization of this drug delivery platform was achieved through concurrent integration of anti-fibrotic efficacy assessment for silybin-RA-loaded micelles and sustained-release kinetic studies of silybin B within the LIP/RSC system (Fig. 1b).

2. Materials and methods

2.1 Materials

1,2-Distearoyl-*sn-glycero*-3-phosphoethanolamine-*N*-[amino (polyethylene glycol)-2000 (ammonium salt)] (DSPE-PEG2000-NH_2), retinoic acid (RA), 4-dimethylaminopyridine (DMAP), and *N*-hydroxysuccinimide (NHS) were purchased from Aladdin (Shanghai, China). 1,2-Dioleoyl-3-trimethylammonium propane chloride (DOTAP chloride) was obtained from Croda (Snaith, UK). Collagenase I was purchased from Invitrogen (Carlsbad, USA). Traut's reagent and silybin B were acquired from Macklin (Shanghai, China). PPC capsules were obtained from Sanofi (Paris, France). Amicon® Ultra centrifugal filters (10 kDa MWCO) were purchased from Merck (Darmstadt, Germany). 1,1′-Dioctadecyl-3,3,3′,3′-tetramethylindotricarbocyanine iodide (DiR) and 3,3′-dioctadecyloxacarbocyanine perchlorate (DiO) were obtained from MedChemExpress (Shanghai, China). Dulbecco's modified Eagle's medium (DMEM), minimum essential medium (MEM), and trypsin solution (0.25%) were obtained from Gibco (Burlington, Canada). Cell Counting Kit-8 (CCK-8) was purchased from GlpBio (Montclair, USA). Fetal bovine serum (FBS) was acquired from ABW (Shanghai, China). Enzyme-linked immunosorbent assay (ELISA) kits (96-well) for collagen type I (Col I) and the tissue inhibitor of metalloproteinases 1 (TIMP1) were obtained from Elabscience (Wuhan, China). All other chemicals and reagents of the highest purity available were obtained from commercial sources.

2.1.1 Preparation of RA-conjugated phosphatidylcholine (RA-DSPE-PEG2000). DSPE-PEG2000-NH_2 (50 mg), RA (100 mg), and 1-ethyl-3-(3-dimethylaminopropyl)carbodiimide (EDC, 50 mg) were dissolved in 10 mL of dichloromethane (CH_2Cl_2) under nitrogen protection. The reaction mixture was stirred at 25 °C for 48 h. Solvent exchange was performed by dialysis (2 kDa MWCO membrane) against ethanol (3 × 2 L) for 24 h. Residual unreacted DSPE-NH_2, RA, and EDC were eliminated through sequential ultrafiltration (30 kDa MWCO). The final product (RA-DSPE-PEG2000) was obtained by rotary evaporation under reduced pressure.

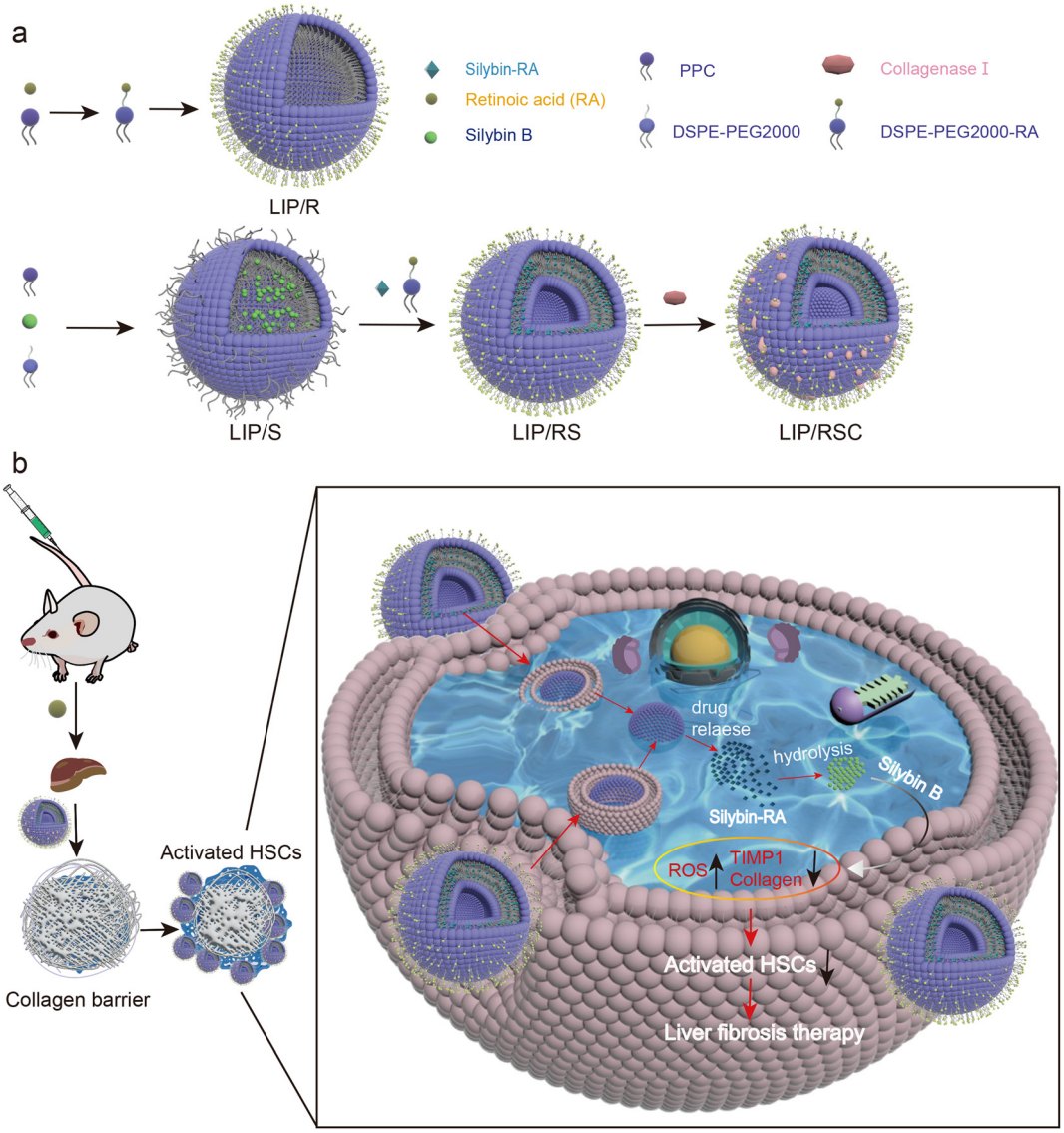

Fig. 1 (a) Schematic illustration of dual RA-functionalized liposomal nanomicelles. (b) Schematic illustration of the proposed destiny of dual RA-functionalized liposomal nanomicelles *in vivo*. The ability of LIP/RSC to penetrate collagen barriers and target activated HSCs facilitates the intracellular release of silybin-RA. Following hydrolysis of silybin B, the TIMP1 expression is suppressed, enhancing ECM collagen degradation, while increased ROS activity induces apoptosis in activated HSCs, ultimately ameliorating liver fibrosis.

2.1.2 Preparation of the RA-modified silybin B complex (silybin-RA). Silybin B (100 mg) in dimethyl sulfoxide (DMSO, 5 mL) was combined with RA (100 mg) activated by EDC/NHS (molar ratio 1 : 1, total 100 mg) in CH_2Cl_2 (10 mL). The cross-linking reaction proceeded at 25 °C with vigorous stirring (800 rpm) for 48 h. Post-reaction purification involved dialysis (500 Da MWCO) against deionized water (3 × 2 L, pH 6.8) for 24 h. Lyophilization yielded the silybin-RA conjugate.

2.1.3 Preparation of SH-collagenase I. Thiolated collagenase I was prepared *via* Traut's reaction by adding 5 × Traut's reagent (dissolved in PBS) to a 5 mg mL^{-1} collagenase I solution. The mixture was stirred at room temperature for 1 h. After the reaction, thiolated collagenase I (SH-collagenase I) was purified using a desalting column (Thermo Fisher Scientific, Waltham, Massachusetts, USA) and used immediately.

2.2 Preparation of cationic liposomal nanomicelles

Two PPC capsules were opened, and their contents were extracted and rinsed with CH_2Cl_2. DOTAP and cholesterol (Chol) were individually dissolved in CH_2Cl_2.[40] Subsequently, DSPE-PEG2000-RA (12 mg), glycerol monostearate (100 mg), and glycerol tricaprylate (100 mg) were subsequently dissolved in CH_2Cl_2. Separately, the prepared silybin-RA (30 mg) was dissolved in CH_2Cl_2. The solutions were combined and homogenized using a rotary evaporator. Organic solvents were evaporated under reduced pressure at 50 °C to form a lipid film, with residual solvents removed by freeze-drying under vacuum. For

the hydration process, 9 mL of PBS was added to the lipid membrane, followed by rotation at 200 rpm and 37 °C for 3 hours to facilitate phase transition and liposome formation. Subsequently, 1 mL of PBS containing collagenase I was introduced for further treatment. The mixture was subjected to pulsed sonication (60% power, 5 s on/5 s off cycles, 30 min) to obtain homogeneous blank liposomal nanomicelles (10 mM lipid concentration).

The liposomes (LIP) were dialyzed against PBS (pH 7.4, MWCO 14 kDa) with magnetic stirring (1 h, ambient temperature), then 40-fold diluted with PBS and centrifuged (2000*g*, 4 °C) using centrifugal filters (10 kDa MWCO) to achieve target volumes.[34]

2.3 Characterization of cationic liposomal nanomicelles

The morphology of cationic liposomal nanomicelles was characterized using an HT-7800 transmission electron microscope (TEM, Hitachi, Tokyo, Japan). The samples were deposited onto formvar-coated copper grids, air-dried under ambient conditions, and subsequently negatively stained with a 2% (w/v) aqueous solution of phosphomolybdic acid.

The intensity-average hydrodynamic diameter, polydispersity index (PDI), and zeta potential values of cationic liposomal nanomicelles were measured using a Malvern ZSU3100 analyzer (Malvern Panalytical Ltd, UK) at a nanoparticle concentration of 1 mg mL^{-1}.

2.4 Quantification tests

RA displays a maximum absorption peak at 328 nm, enabling spectral identification of compounds containing the RA moiety. Based on this characteristic, 99% pure RA was utilized as the reference standard for spectrophotometric quantification. The total RA content (RA-DSPE-PEG2000 and silybin-RA) was determined by constructing a calibration curve relating the absorbance intensity to the RA concentration. Full-wavelength scans (200–700 nm) using a microplate reader revealed compound-specific absorption peaks that closely aligned with those of pure silybin B in comparative analysis (wavelength deviation: $\leq \pm 2$ nm). Absorbance values at target wavelengths were subsequently linked with drug concentrations. For quantification, unbound and released silybin B was quantified using high-performance liquid chromatography (HPLC), while the collagenase I levels were measured with a Bradford Protein Assay Kit. Four liposomal micelle formulations were evaluated in triplicate with parallel measurements to ensure reproducibility.

2.5 Cell culture

The human hepatocyte (WRL68) and human liver stellate (LX-2) cell lines were purchased from Hangzhou Lingjun Biotechnology Co. Ltd. (Hangzhou, China). WRL68, LX-2 and carbon tetrachloride (CCl_4)-activated LX-2 cells (LX-2-CCl_4) were cultured in DMEM supplemented with 10% (v/v) FBS, 100 μg mL^{-1} of streptomycin and 100 U mL^{-1} of penicillin at 37 °C under a 5% CO_2 humidified atmosphere.

2.6 Cell survival assay

WRL68, LX-2 and LX-2-CCl_4 cells were seeded in 96-well plates (6×10^3 cells per well, 200 μL of growth medium) for 12 h. The culture medium was replaced with a serum-free medium containing gradient concentrations of liposomal nanomicelles. After 24 or 48 h treatment, 20 μL of CCK-8 reagent (5 mg mL^{-1} in PBS) was added per well. Following incubation for 4 h in the dark at 37 °C, the medium was aspirated and formazan crystals were dissolved in 150 μL of DMSO. Absorbance (450 nm) was measured using a multi-mode microplate reader (SynergyLX, BioTek, USA). Untreated cells served as controls, with quadruplicate technical replicates per condition.

2.7 Release of silybin B from LIP/RSC *in vitro*

LX-2-CCl_4 and WRL68 cells were seeded in 10 cm dishes (5×10^5 cells per dish) for 24 h. The medium was replaced with a serum-free medium containing LIP/RSC and incubated for 2 h. The cells were washed with PBS (3×), harvested, and processed for quantification. Cellular lysates were prepared using lysis buffer, followed by silybin B extraction in methanol. After centrifugation (12 000*g*, 10 min), the supernatants were subjected to lyophilization and reconstitution in the mobile phase for HPLC quantification of silybin B.

2.8 Tropism and uptake of cationic liposomal nanomicelles under the collagen type I barrier *in vitro*

Cy3-silybin-RA was synthesized through DCC/HBOT-mediated conjugation between silybin-RA and Cy_3-COOH. LX-2 cells were seeded onto 35 mm cell culture slides (5×10^4 cells per slide, 1 mL of medium per slide) for 24 h. After medium removal, the cells were treated with 1 mL of serum-free medium containing Cor6 formulations (free Cor6, LIP/S/Cor6, LIP/R/Cor6, LIP/RS/Cor6, and LIP/RSC/Cor6; Cor6: 0.025 μg per slide). Post-treatment, the cells were subjected to PBS rinsing (3×), 4% paraformaldehyde fixation, and DAPI counterstaining in antifade mounting medium. Confocal imaging was performed using a Leica DMi8 system (Leica Biosystems, Germany), with fluorescence intensity quantified using ImageJ software.

2.9 Immunofluorescence staining of collagen I *in vitro*

LX-2 or WRL68 cells were fixed with 4% paraformaldehyde in PBS (30 min, RT), and then washed with PBS (3×). After blocking with 5% goat serum/PBS (1 h, RT), the cells were incubated with rabbit anti-human collagen I primary antibody (Abcam, UK; in blocking buffer) overnight at 4 °C. Following equilibration to RT, cells were washed with PBS (3×) and incubated with Cy3-conjugated donkey anti-rabbit IgG secondary antibody (ZSGB-Bio, China) for 1 h at 37 °C. Following the final PBS wash, nuclei were counterstained with DAPI and the specimens were mounted with antifade medium. Confocal imaging was conducted using a DMi8 CLSM (Leica Biosystems, Germany), with per cell Cy3-collagen I fluorescence intensity quantified using ImageJ software.

2.10 Intracellular distribution

LX-2 cells were seeded in glass-bottomed 35 mm dishes (1×10^4 cells per dish, 1 mL of medium) for 12 h. Subsequently, the medium was replaced with an LIP/RSC/Cor6-supplemented serum-free medium (Cor6: 0.05 μg per dish). After 2 h of incubation, the cells were subjected to PBS washing (3×) and then stained with FluoLyso™ Red (100 nM; Uelandy, China) for 1 h at 37 °C. Fixed cells (4% paraformaldehyde) were counterstained with DAPI and mounted with antifade medium. CLSM was performed using a DMi8 system (Leica Biosystems, Germany). Quantitative analysis of the mean fluorescence intensity per cell was conducted using ImageJ software.

2.11 Animals

2.11.1 Animal ethical approval statement. Female BALB/c mice (6–8 weeks old, 20 ± 2 g; n = 110) were purchased from SPF Biotechnology Co., Ltd (Beijing). Mice were individually housed under controlled conditions (12 h/12 h light/dark cycle, lights on 06:00) with *ad libitum* access to food/water. All experimental protocols were approved by the Second Affiliated Hospital of Xiamen Medical College (Ethics No. 2024004) and conducted in compliance with the ARRIVE guidelines,[41] adhering to institutional regulations of the Laboratory Animal Center.

2.11.2 Animal treatment. CCl_4-induced liver fibrosis model mice (n = 6 per group) were maintained on standard chow with free water access. The fibrotic group received twice-weekly intraperitoneal CCl_4/olive oil injections (1 : 7 v/v, 2.5 μL g^{-1}) for 6 weeks, whereas mice in the control group received olive oil intraperitoneally.[40]

2.12 Hemolysis assay

Heparin-coated microcentrifuge tubes were used to collect 5 mL murine whole blood through retro-orbital sinus puncture. The anticoagulated blood was diluted 10-fold with heparin-supplemented PBS. Erythrocyte suspensions (600 μL) were vortex-mixed with 400 μL of gradient concentrations of liposomal nanomicelles and incubated (37 °C, 6 h). The post-incubation samples were centrifuged (1000g, 5 min). The supernatants were collected for hemoglobin quantification through absorbance measurement at 560 nm.

The hemolysis percentage was calculated as:

$$\text{Hemolysis percentage}\,(\%) = \left(\mathrm{OD}_{\text{experimental group}} - \mathrm{OD}_{\text{negative control group}}\right) / \left(\mathrm{OD}_{\text{positive control group}} - \mathrm{OD}_{\text{negative control group}}\right) \quad (1)$$

2.13 Acute toxicity study

The acute toxicity of LIP/RSC was assessed by daily intravenous administration (35 μM, 200 μL) to healthy BALB/c mice for three consecutive days. Control groups received equivalent-volume PBS injections. 24 h post-final administration, the euthanized mice were subjected to organ harvest (heart, liver, spleen, lungs, and kidneys) with 4% paraformaldehyde for subsequent histological analyses.

2.14 Drug distribution and metabolism in the body

2.14.1 *In vivo* imaging. For biodistribution assessment, DiR-labeled micellar formulations (LIP/S/DiR, LIP/R/DiR, LIP/RS/DiR, and LIP/RSC/DiR) were substituted for therapeutic agents. The fibrotic/healthy control mice (n = 3 per group) received tail vein-injected DiR (1 mg kg^{-1} in 100 μL of PBS). Longitudinal monitoring was conducted using a Lumina XRMS system (PerkinElmer) with 745/800 nm excitation/emission wavelengths at defined intervals (4, 8, 24, 48, and 72 h post-administration) with 2% isoflurane anesthesia. Terminal imaging (72 h) combined cervical dislocation with organ-specific fluorescence quantification under standardized parameters.

2.14.2 Pharmacokinetic analysis. LIP/S, LIP/RS and LIP/RSC were intravenously administered to healthy mice *via* tail vein injection. Blood and liver tissues were collected at predetermined intervals (1–72 h post-administration). Serum isolation was performed through a two-step process: initial coagulation (30 min, 25 °C) followed by centrifugation (3000 rpm, 10 min). Liver specimens were snap-frozen in liquid nitrogen, cryopulverized, and homogenized in an ice bath to yield a 10% tissue suspension (9 : 1 saline : tissue). Homogenate–methanol (2 : 1, v/v) mixtures were centrifuged (2500 rpm, 10 min), with precipitates washed (methanol 3×) and supernatants lyophilized post-evaporation.

Serum and hepatic lysates were subjected to optimized liquid–liquid extraction using methanol : ethyl acetate (3 : 7, v/v). Precise aliquots of 1.5 mL of solvent were dispensed in 500 μL of matrix using calibrated pipettes. Phase separation was achieved through rigorous vortexing (3000 rpm, 3 min) and centrifugation (4000g, 20 min, 4 °C), and organic phases were transferred *via* salinized capillaries, concentrated (<50 μL) *via* nitrogen/vacuum evaporation, and vortex reconstituted (30 s × 3) in methanol.

Silybin B was quantified using HPLC-UV (Agilent 1620, C18, 5 μm) with an isocratic eluent (methanol : 1% acetic acid = 45 : 55, flow rate: 1.0 mL min^{-1}, column temperature: 25 °C, and UV detection at 287 nm). Reference standards were gravimetrically prepared (1.000 mg).

2.15. Serum cytokines, ELISA assays and hydroxyproline measurements

Serum cytokines were measured using commercial ELISA kits (Beyotime Biotechnology, Shanghai, China) according to the manufacturer's instructions.

The contents of Col I and TIMP1 were measured using commercial ELISA kits (Col I: E-EL-M0325; TIMP1: E-EL-M3071, Wuhan, China) according to the manufacturer's instructions.

The content of hydroxyproline (Hyp) was measured using a hydroxyproline assay kit (Jiancheng Biotech) according to the manufacturer's instructions.

2.16 Histological analyses

Paraffin-embedded liver tissues were sectioned with 3 μm thickness. After deparaffinization and hydration, sections were

stained using an H&E staining kit (Hematoxylin–Eosin Stain Kit, Cat: G1120, Solarbio, Beijing, China) or 0.1% (w/v) Sirius Red (Modified Sirius Red Stain Kit, Cat: G1472, Solarbio, Beijing, China) in a saturated aqueous solution of picric acid for 1 h. Slides were then rinsed twice in 0.01 M HCl for 15 min each to remove unbound dye. After dehydration, slides were mounted and photographed. Sections were also stained using a Masson's trichrome staining kit (Modified Masson's Trichrome Stain Kit, Cat: C0189S, Beyotime, Shanghai, China) according to the manufacturer's instructions.[20]

2.17 Statistical analysis

All experiments were repeated at least three times. All data are presented as the means ± standard deviation (SD) and were analyzed using ordinary one-way/two-way analysis of variance ANOVA and unpaired tests. Statistical analyses were performed using GraphPad 9.4.1. P values < 0.05 were considered statistically significant; individual P values are indicated in figure legends.

3. Results and discussion

3.1 Characterization of cationic liposomal nanomicelles

In this study, four types of PPC-based cationic liposomal nanomicelles were prepared using sequential loading strategies. These formulations included silybin B-loaded liposomes (LIP/S), RA-loaded liposomes (LIP/R), dual-loaded liposomes containing RA and silybin B (LIP/RS), and triple-loaded liposomes incorporating RA, silybin B, and collagenase I (LIP/RSC, Fig. 1). The structural integrity of all formulations was systematically verified through ultraviolet-visible spectroscopy (UV-vis), Fourier transform infrared (FT-IR) spectroscopy, and nuclear magnetic resonance (NMR) characterization (SI Fig. S1–S4).

The structural characteristics and dimensional profiles of LIP/S, LIP/R, LIP/RS, and LIP/RSC formulations were systematically investigated through transmission electron microscopy (TEM) and dynamic light scattering (DLS) analyses. TEM imaging revealed uniformly spherical nanostructures across all formulations, while the hydrodynamic diameters determined through DLS analysis were 78.7 ± 3.9 nm (LIP/S), 97.2 ± 1.7 nm (LIP/R), 87.1 ± 2.6 nm (LIP/RS), and 67.6 ± 2.3 nm (LIP/RSC) (Fig. 2a–d). The nanoscale vesicular architecture with its distinct spherical morphology was confirmed by TEM micrographs, demonstrating >90% monodisperse particle distribution below 100 nm as evidenced by corresponding histogram analyses. Moreover, the RA-coupled liposomes (LIP/R) (Fig. 2e) exhibited increased vesicular dimensions characterized by electron-dense peripheral layers, likely attributed to RA conjugation. LIP/R, LIP/RS and LIP/RSC exhibited well-defined core–shell structures. The LIP/RS architecture showed continuous membrane encapsulation of core-localized nanoparticles (Fig. 2f), while collagenase I-encapsulated LIP/RSC demonstrated preserved core nanoparticles with distinct proteinaceous surface coatings (Fig. 2g), indicating multivesicular organization.

DLS measurements revealed larger hydrodynamic diameters (140.6 ± 1.6 nm for LIP/S, 174.8 ± 2.1 nm for LIP/R, 142.0 ± 1.6 nm for LIP/RS, and 94.9 ± 6.3 nm for LIP/RSC, Fig. 2h) and the surface zeta potential values were 20.3 ± 1.1 mV, 24.6 ± 0.1 mV, 22.6 ± 2.4 mV, and 20.5 ± 0.6 mV, respectively (Fig. 2i). The observed discrepancy in size between the TEM and DLS results is attributed to hydration-induced swelling during DLS analysis. All formulations demonstrated excellent aqueous dispersibility, as evidenced by polydispersity indices (PDIs) below 0.5 (predominantly in the range of 0.2–0.3).

Under physiological conditions (DMEM supplemented with 10% FBS, 37 °C), obtained TEM images, as displayed in Fig. 3a–d, show that all liposomal formulations maintained colloidal stability over 7 days with <5% size variation, while extended evaluation (30 days) revealed controlled size increases (from 67.6 ± 2.3 nm to 92.1 ± 3.8 nm for LIP/RSC) and yet preserved surface charge homogeneity (20.5 ± 0.6 mV to 19.2 ± 1.1 mV) (Fig. 3e and f). Quantitative characterization demonstrated effective payload retention: RA across formulations (LIP/R: 347.4 ± 16.9 μg mL^{-1}; LIP/RS: 339.9 ± 12.9 μg mL^{-1}; LIP/RSC: 367.4 ± 7.7 μg mL^{-1}, Fig. 3g); collagenase I in LIP/RSC (2.23 ± 0.07 mg mL^{-1} using the BCA assay, Fig. 3h); and silybin derivatives (LIP/S: 305.3 ± 17.1 μg mL^{-1}; LIP/RS & LIP/RSC co-loading: 308.3 ± 37.1 μg mL^{-1} and 309.1 ± 18.8 μg mL^{-1}, respectively, Fig. 3i).

The biocompatibility of liposome nanomicelles was assessed in three human hepatic cell lines (hepatocytes: WRL68, HSCs: LX-2, and activated HSCs: LX-2-CCl_4) using the CCK-8 assay kit. After 48 h of incubation, the viability of all cell types was higher than 80% at concentrations below 0.1 mM, demonstrating good biocompatibility of these drug-free LIP nanomicelles at these concentrations (SI Fig. S5). Cell viability following administration of silybin-RA and LIP/RSC-loaded silybin-RA was evaluated using the CCK-8 assay kit after 24 h of incubation. Then "curve fitting" was performed using the "[Inhibitor] *versus* Normalized Response – Variable Slope" model in the "Nonlinear Regression (Curve Fit)" module, and half-maximal inhibitory concentration (IC_{50}) values were calculated.

The free silybin-RA exhibited IC_{50} values of 36.77 μM (LX-2-CCl_4), 59.14 μM (LX-2), and 72.37 μM (WRL68) (Fig. 3j). Notably, the LIP/RSC formulation exhibited enhanced levels of cellular toxicity toward HSC populations, yielding IC_{50} values of 35.62 μM (LX-2-CCl_4) and 45.73 μM (LX-2), while showing reduced hepatocyte toxicity with an IC_{50} value of 83.63 μM (WRL68) (Fig. 3k).

3.2 Intracellular distribution of liposomal nanomicelles

Carbon tetrachloride (CCl_4)-activated LX-2 hepatic stellate cells (LX-2-CCl_4) exhibited characteristic collagen deposition patterns. Biochemical assays revealed a 2.5-fold increase in the total collagen content in LX-2-CCl_4 compared to WRL68, with a 1.7-fold increase compared to unstimulated LX-2 controls (SI Fig. S6). Immunofluorescence quantification confirmed progressive collagen I accumulation, showing a 3.6-fold higher

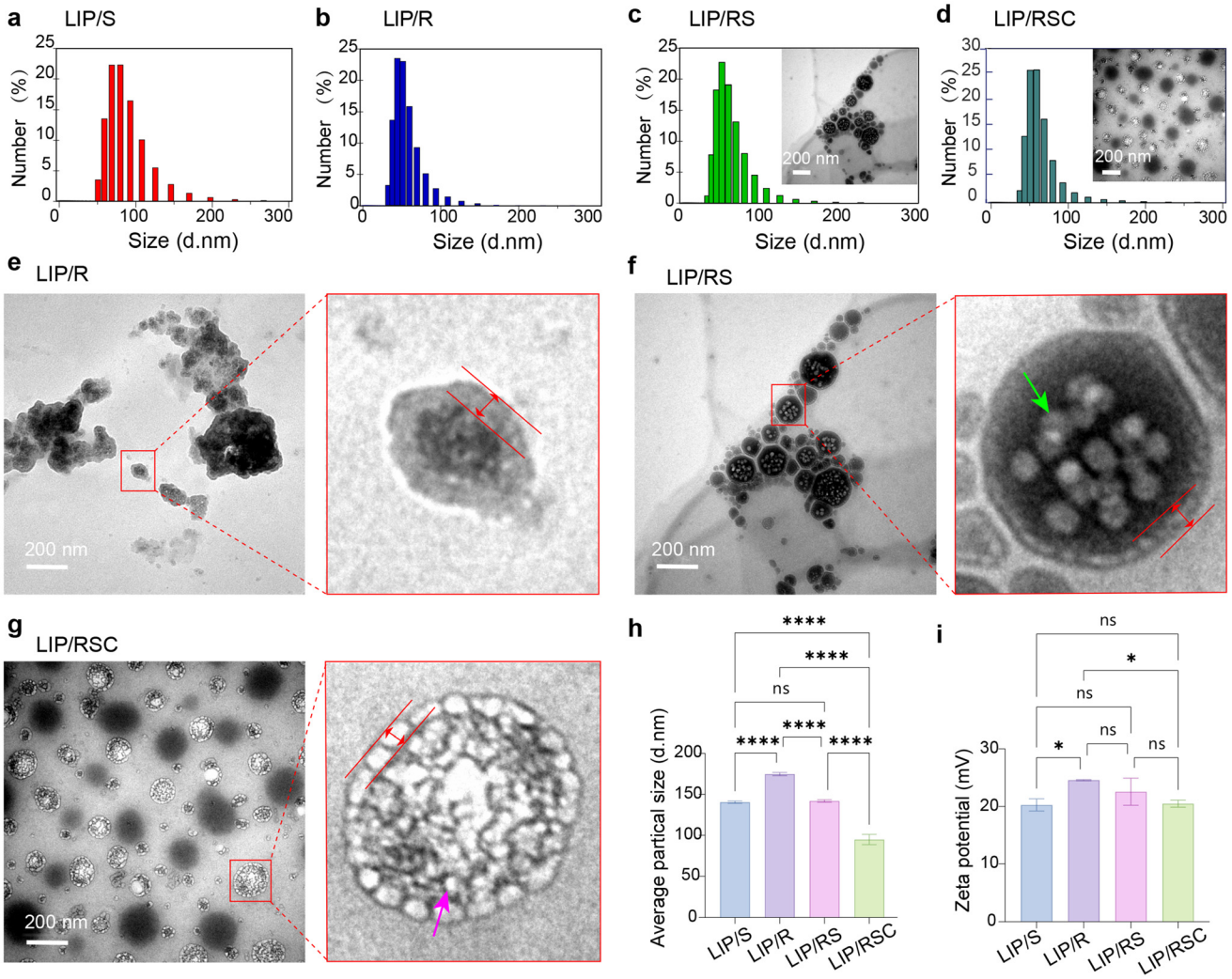

Fig. 2 Morphological characteristics of cationic liposomal nanomicelles. Representative TEM images of different LIP micelles: (a) LIP/S, (b) LIP/R, (c) LIP/RS and (d) LIP/RSC. Microstructures of LIP/R, LIP/RS and LIP/RSC obtained using TEM, where the right-hand panel shows a magnified view of the particles within the red box in the left-hand panel and the red lines indicate the shell structure: (e) LIP/R; (f) LIP/RS where the green arrow highlights the core contents; and (g) LIP/RSC Where the purple arrow marks the core contents. (h) Hydrodynamic size distribution of different LIP micelles determined by DLS. (i) Zeta potential of different LIP micelles in phosphate-buffered saline (PBS, pH 7.4). The data are expressed as the mean ± SD. Error bars: $*P < 0.05$ and $****P < 0.0001$; "ns", no significant difference.

intensity in LX-2 *versus* WRL68, further increasing to 1.7-fold in LX-2-CCl_4 with results validated by CLSM imaging coupled with ImageJ analysis (Fig. 4a and b).

Liposomal micelle pretreatment significantly inhibited Col I expression in LX-2 cells. Quantitative analysis demonstrated that 4 h LIP/RSC exposure induced physiologically relevant collagen degradation in LX-2-CCl_4 models, showing 27.1% superior efficacy with respect to LIP/RS controls ($P < 0.05$, Fig. 4c). Through the synergistic action of silybin B and PPC, and aided by collagenase I-mediated incision, LIP/RSC achieved a 55.9% total collagen reduction (*vs.* untreated LX-2-CCl_4, Fig. 4c) and 84.9% specific Col I depletion (Fig. 4d and e), significantly enhancing fibrotic matrix penetration. The RA component facilitates targeted enzymatic degradation of collagen, thereby inhibiting the formation of pathological fibrosis.

3.3 Anti-Col I activity of liposomal nanomicelles *in vitro*

Type I collagen is the most abundant ECM protein and forms the primary component of fibrotic scar tissue in liver fibrosis. To evaluate the LX-2 cellular uptake of Cor6-loaded liposomal nanomicelles, we established an *in vitro* model by pre-coating Transwell membranes with Col I (Fig. 5a), reflecting its predominant role in fibrotic ECM.

Sulfo-cyanine3 (Cy3) exhibits specific red fluorescence emission (λ_{em}: 550–600 nm) upon laser excitation, showing minimal spectral overlap with the green fluorescence of Cor6-LIP (λ_{em}: 500–550 nm). This distinct optical signature enables precise detection using CLSM. Based on the optimal physicochemical characteristics of Cy3-silybin-RA conjugates, we propose evaluating the scissors-like functionality exhibited by

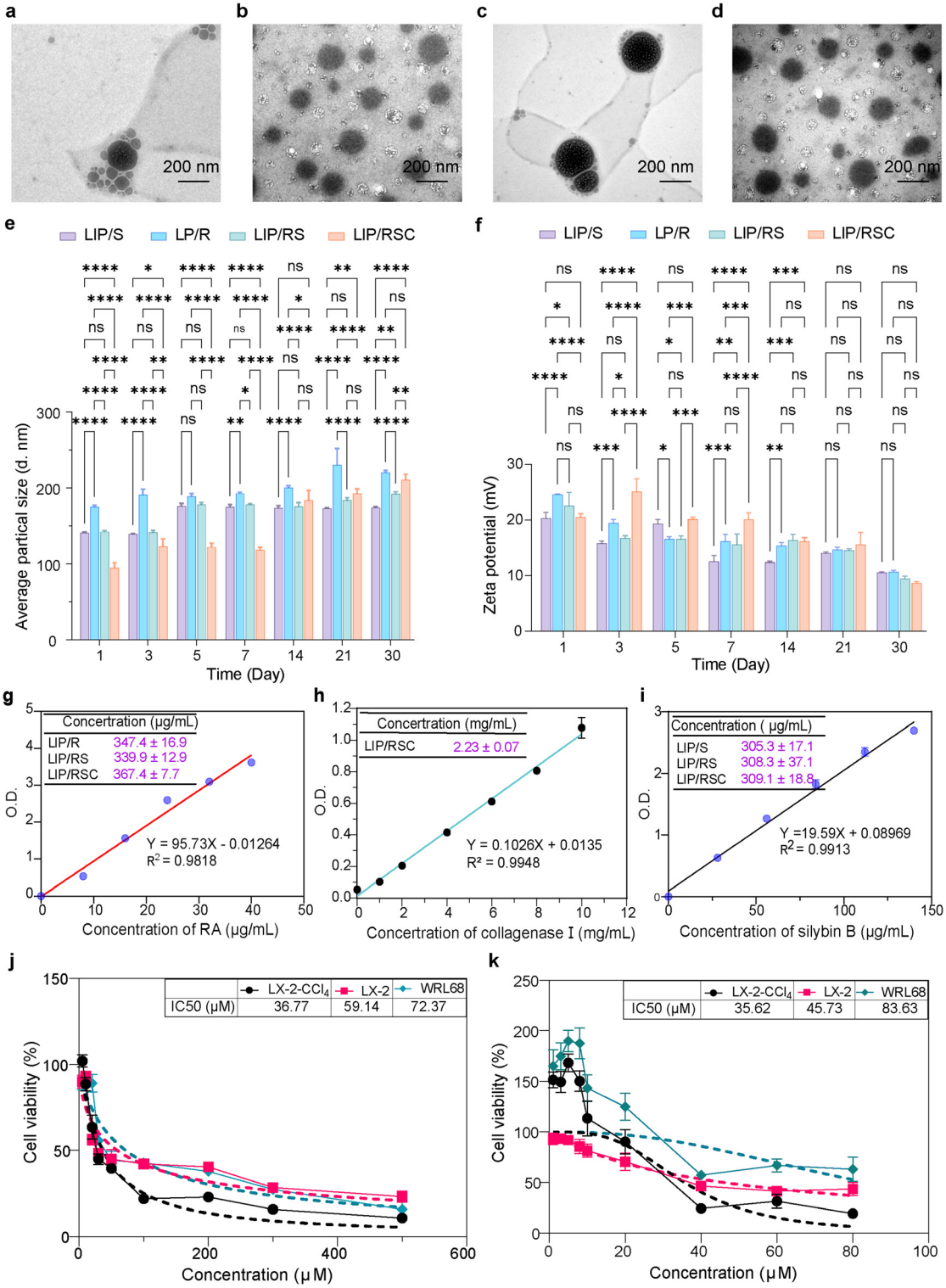

Fig. 3 Morphological characteristics of cationic liposomal nanomicelles. Representative TEM images of different LIP micelles obtained after 30 days: (a) LIP/S, (b) LIP/R, (c) LIP/RS and (d) LIP/RSC. (e) Size stability of LIP micelles in DMEM supplemented with 10% fetal bovine serum (FBS) at 37 °C. (f) Zeta potential variations under identical conditions. (g) Quantification of RA loading using UV-vis spectroscopy at 328 nm. (h) Collagenase I content determined by the BCA protein assay. (i) Co-quantification of silybin-RA using UV-vis spectroscopy at 287 nm. IC_{50} values of LX-2-CCl_4, LX-2, and WRL68 cells obtained after 24 h of treatment: (j) silybin-RA and (k) LIP/RSC nanomicelles. The data are expressed as the mean ± SD. Error bars: *P < 0.05, **P < 0.01, ***P < 0.001, and ****P < 0.0001; "ns", no significant difference.

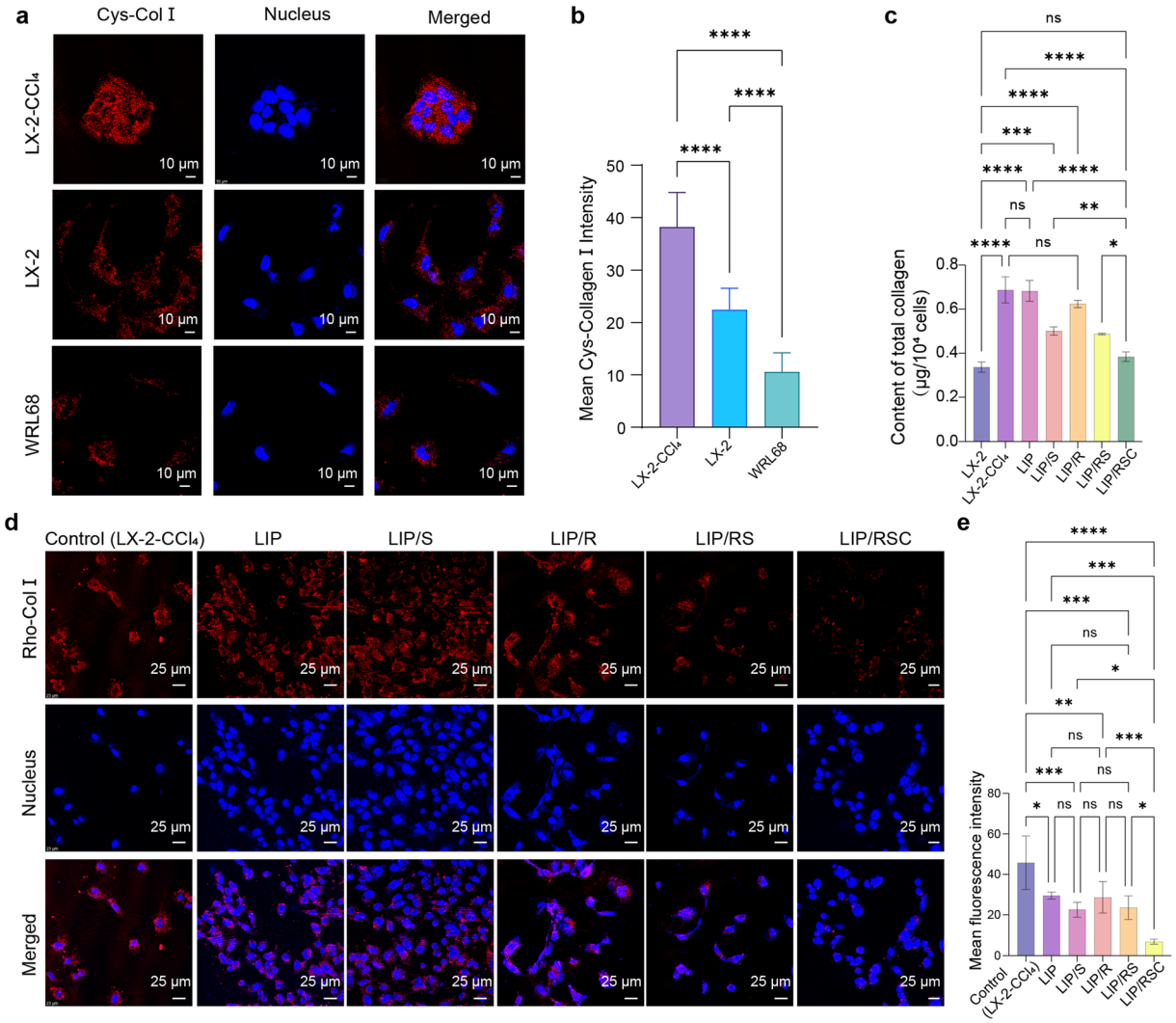

Fig. 4 Cellular uptake of LIP nanomicelles *in vitro*. (a) CLSM images of collagen I immunostaining (red) in WRL68, LX-2 and LX-2-CCl_4 cells. (b) Fluorescence intensity of Cy3-collagen I (Cy3-Col I) in WRL68, LX-2 and LX-2-CCl_4 cells, quantified using ImageJ software (n = 10). (c) Total collagen content in LX-2-CCl_4 cells treated with LIP micelles for 4 h (n = 3). (d) CLSM images of collagen I immunostaining (red) in LX-2-CCl_4 cells pre-incubated for 4 h with different Cor6-loaded LIP micelles. (e) Mean fluorescence intensity of LX-2-CCl_4 cells treated with LIP micelles for 4 h, measured using ImageJ software (n = 10). The data in (b), (c) and (e) are presented as the mean ± SD. Error bars: *P < 0.05, **P < 0.01, ***P < 0.001, and ****P < 0.0001; "ns", no significant difference.

the engineered liposomal nanomicelle system. Following successful characterization, Cy3 was covalently conjugated to the hydroxyl group of silybin-RA *via* carbodiimide chemistry.

To establish a biomimetic collagen barrier model, LX-2 cells were first cultured on collagen-coated plates, after which Cor6-labeled LIP nanomicelles were directly applied. Subsequently, multiple Cor6-loaded LIP formulations were introduced, and comprehensive analysis *via* CLSM coupled with ImageJ software assessed LX-2 cellular uptake and Cy3-silybin-RA degradation over the course of 2 h. Cellular accumulation analysis revealed comparable drug uptake of free Cor6, LIP/Cor6, LIP/R/Cor6, and LIP/RS/Cor6 (Fig. 5b), confirming the barrier effect of Col I on nanoparticle penetration. Notably, LIP/RSC/Cor6 exhibited superior accumulation *via* collagenase I-mediated matrix degradation. Retinol-modified constructs (LIP/R/Cor6 and LIP/RS/Cor6) showed enhanced LX-2 targeting, consistent with retinol transport receptor overexpression in these cells,[42–44] as established by previous studies.[45–48] Quantitatively, collagenase I-containing LIP/RSC achieved 10-fold higher intracellular accumulation than the non-enzymatic variants (LIP/S, LIP/R, and LIP/RS), demonstrating the barrier role of Col I in nanoparticle internalization (Fig. 5c). Flow cytometry revealed uptake patterns of Cor6-modified nanomicelles that differed between activated LX-2-CCl_4 and WRL68 cells (Fig. 5d–f), while HPLC analysis confirmed enhanced silybin-RA release kinetics in LX-2 cells, demonstrating 4-fold higher absorption and release rates compared to WRL68 (SI Fig. S7). These findings collectively demonstrate

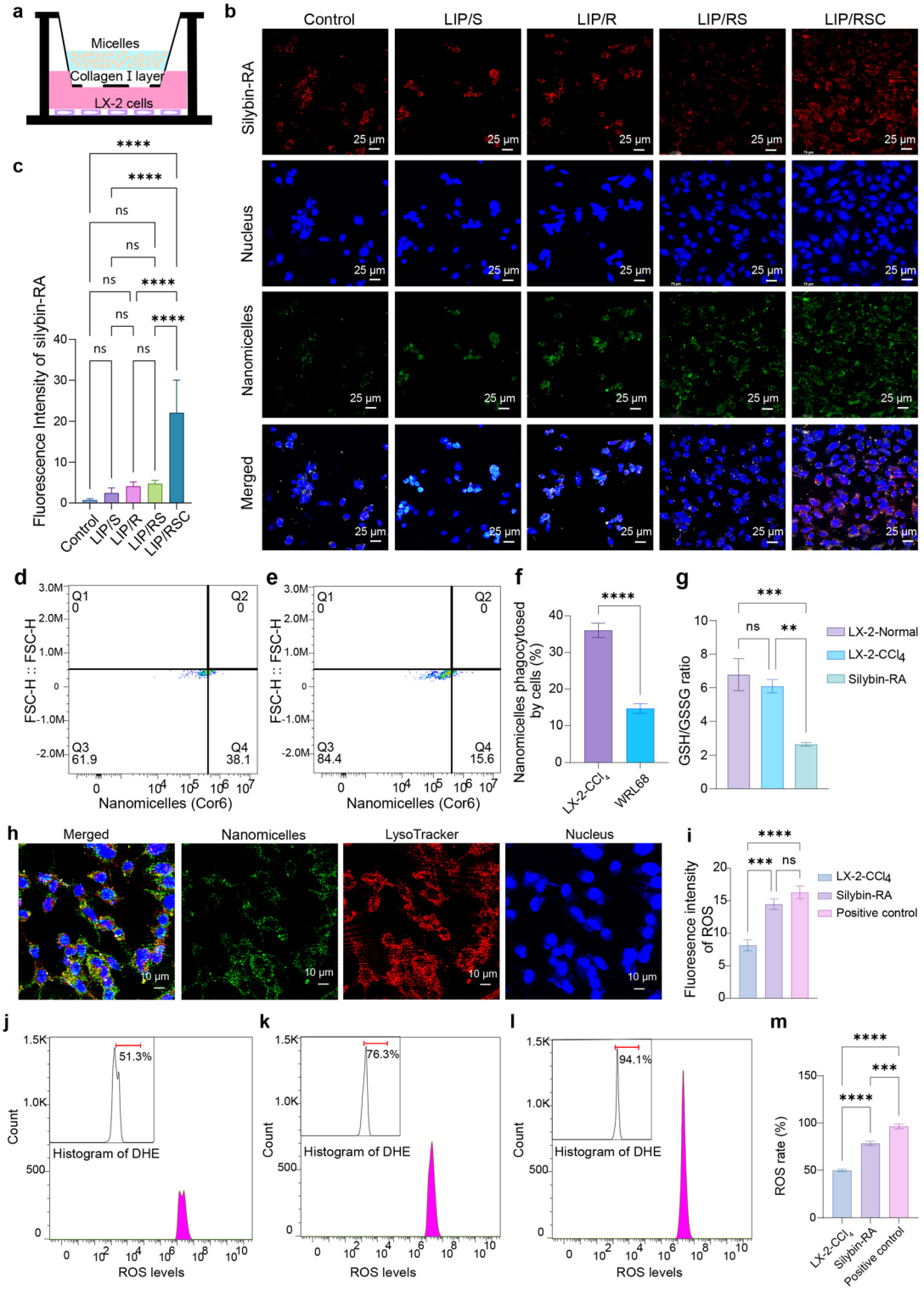

Fig. 5 Anti-Col I activity of liposomal nanomicelles with silybin-RA in HSCs *in vitro*. (a) Schematic of the *in vitro* Col I barrier model mimicking the fibrotic ECM. (b) CLSM images of silybin-RA (red) in LX-2 cells preincubated for 4 h with different Cor6-loaded LIP micelles. (c) Mean fluorescence intensity of internalized silybin-RA, quantified using ImageJ software (n = 10). Absorption situation by flow cytometry in (d) LX-2-CCl_4 and (e) WRL68 cells. (f) Differences in the absorption of nanomicelles in LX-2-CCl_4 and WRL68 cells. (g) GSH/GSSG ratio levels. (h) CLSM images of LysoTracker™ Red in LX-2 cells preincubated for 2 h with Cor6-loaded LIP/RSC. (i) Quantification of intracellular ROS levels using ImageJ software. ROS rate levels as obtained by flow cytometry: LX-2-CCl_4 (j), silybin-RA (k), and positive control (l). (m) Quantification of cellular ROS levels by flow cytometry. The data are the mean ± SD (n = 3). Error bars: $^{**}P < 0.01$, $^{***}P < 0.001$, and $^{****}P < 0.0001$; "ns", no significant difference.

that the therapeutic efficacy of LIP/RSC arises from synergistic collagenase-mediated matrix remodeling and retinol receptor-targeted drug delivery.

To evaluate the intracellular distribution of LIP/RSC/Cor6 in LX-2 cells, CLSM was employed to analyze Cor6 fluorescence colocalization between Cor6 and LysoTracker Red-labeled lysosomes/late endosomes following nanoparticle treatment (Fig. 5h). These experiments revealed strong colocalization of the green fluorescence of Cor6 with the red fluorescence of LysoTracker at 120 min, indicating that LIP/RSC/Cor6 was internalized through the endocytic pathway and eventually became trapped inside lysosomal nanomicelles. These observations indicate that drugs carried by LIP/RSC could achieve good intracellular release.

As expected, the Col I barriers in LIP/RSC/Cor6 groups were clearly degraded, demonstrating that decoration with collagenase I endowed LIP with a nano-scissors-like function that allows better penetration under the conditions of excessive collagen fibrosis. Moreover, studies have demonstrated that LIP nanocarriers, particularly LIP/RSC, exhibit efficient cellular uptake in LX-2 cells with rapid intracellular release within 2 h. These findings suggest that LIP/RSC could act as "nano-scissors" capable of penetrating collagen barriers, thereby enabling prompt intracellular internalization and payload release.

To assess silybin-RA-mediated oxidative effects, the deduced GSH/GSSG (glutathione/glutathione disulfide) ratio subsequently corroborated the activation of oxidative stress (Fig. 5g). Additionally, reactive oxygen species (ROS) generation in activated LX-2-CCl_4 was quantified using dihydroethidium (DHE) fluorescence assays after 24 h of treatment with 35 μM silybin-RA. DHE-stained ROS levels were measured by flow cytometry (Fig. 5j–l) and CLSM. Both flow cytometry (fluorescence intensity: 14.5 ± 0.8 *vs.* 8.2 ± 0.9, $P < 0.001$, Fig. 5i; ROS rate: 78.3 ± 1.3% *vs.* 49.8 ± 1.8%, $P < 0.0001$, Fig. 5m) and confocal imaging (SI Fig. S8) revealed 1.6-fold elevated ROS levels in the treated *versus* control groups. These data suggest that silybin-RA-induced GSH/GSSG ratio depletion promotes ROS accumulation, triggering apoptosis in LX-2-CCl_4 cells and consequently attenuating hepatic fibrogenesis. Molecular analyses revealed silybin-RA coadministration perturbed the redox equilibrium in activated LX-2 cells *via* GSH/GSSG axis modulation.[49,50] Molecular analyses revealed silybin-RA coadministration perturbed the redox equilibrium in activated LX-2 cells *via* GSH/GSSG axis modulation.

3.4 Distribution and metabolism of liposomal nanomicelles *in vivo*

To assess the safety of liposomal nanomicelles, hemocompatibility of LIP/RSC was assessed using hemolytic assays prior to *in vivo* biodistribution studies. Cationic LIP/RSC caused complete hemolysis (100%) at >100 μM (SI Fig. S9). Acute toxicity was examined through 3 days of consecutive intravenous administration of 35 μM LIP/RSC to healthy mice. Post-euthanasia organ analysis using H&E staining showed no observable histopathological abnormalities at the tested doses (SI Fig. S10), validating formulation biosafety.

Comparative biodistribution studies between LIP/RS and LIP/RSC were performed in healthy mice receiving 35 μM formulations intravenously. Real-time imaging tracked spatiotemporal distribution alongside scheduled blood/liver sampling (Fig. 6a). Sirius Red/Masson's trichrome staining (Fig. 6b and c) and ECM collagen quantification (Fig. 6d) revealed CCl_4-induced fibrotic deposition (4–5-fold *vs.* control; $P < 0.001$). Serum and liver ALT/AST levels—validated hepatocellular integrity biomarkers—demonstrated a 5.7-fold increase ($P < 0.0001$) in CCl_4-induced fibrotic mice *versus* controls, with concurrent ALT/AST ratio reduction to 80% of control values (Fig. 6e–g). These enzymatic perturbations confirmed concordant circulatory and parenchymal hepatocyte damage, consistent with the histopathological validation of fibrosis progression.

Distinct pharmacokinetic profiles emerged: the concentration of plasma silybin B decreased gradually within the 2–8 h plateau phase, whereas hepatic accumulation persisted >72 h. LIP/RSC enhanced liver retention of silybin B by 2.1-fold *versus* LIP/RS ($P < 0.001$), maintaining therapeutic levels from 8 to 72 h post-injection (Fig. 6h and i). The addition of collagenase I accelerates the release of silybin B in LIP/RSC at the target site, while the addition of RA forms a bilayer core–shell structure that optimizes the long-term release characteristics. The pharmacokinetic correlation indicates that the integrity of the nanocarriers is maintained during the *in vivo* circulation process, confirming the consistency between the structure and function in the drug release kinetics.

Stage-specific hepatic collagen heterogeneity drove comparative biodistribution analysis using NIR-imaged DiR micelles in age-matched healthy *versus* CCl_4-induced fibrotic mice *via* tail vein administration. Healthy cohorts exhibited universal 8 h hepatic accumulation peaks, with LIP/RSC sustaining >72 h retention through retinol-driven stellate cell targeting, whereas fibrotic models exhibited progressive loss of formulation differentiation (2 h–3 d post-injection) and delayed LIP/RSC pharmacokinetics (24 h peak with 0.18 h^{-1} clearance rate), reflecting collagen barrier-hindered permeation and impaired metabolic clearance. Both cohorts retained prolonged LIP/RSC/DiR persistence ($P < 0.001$, intergroup), establishing fibrosis stage-dependent equilibrium modulated by hepatic metabolic adaptation and nanocarrier surface characteristics (SI Fig. S11a and b). The divergent maximum accumulation and peak time patterns between healthy mice and CCl_4-treated groups reflect tripartite equilibrium dynamics among hepatic fibrosis severity, metabolic clearance capacity, and micelle surface properties. *Ex vivo* whole-organ imaging at 72 h post-administration (Fig. 7a) revealed liver-dominant biodistribution ($P < 0.0001$; Fig. 7b and c), with LIP/RSC/DiR and LIP/RS/DiR showing 2.3×/1.4× liver signal amplification *versus* LIP/S/DiR in fibrotic models ($P < 0.0001$; Fig. 7c). The RA-modified delivery system achieved enzyme-responsive sustained release, achieving targeted hepatic retention with reduced dosage frequency.

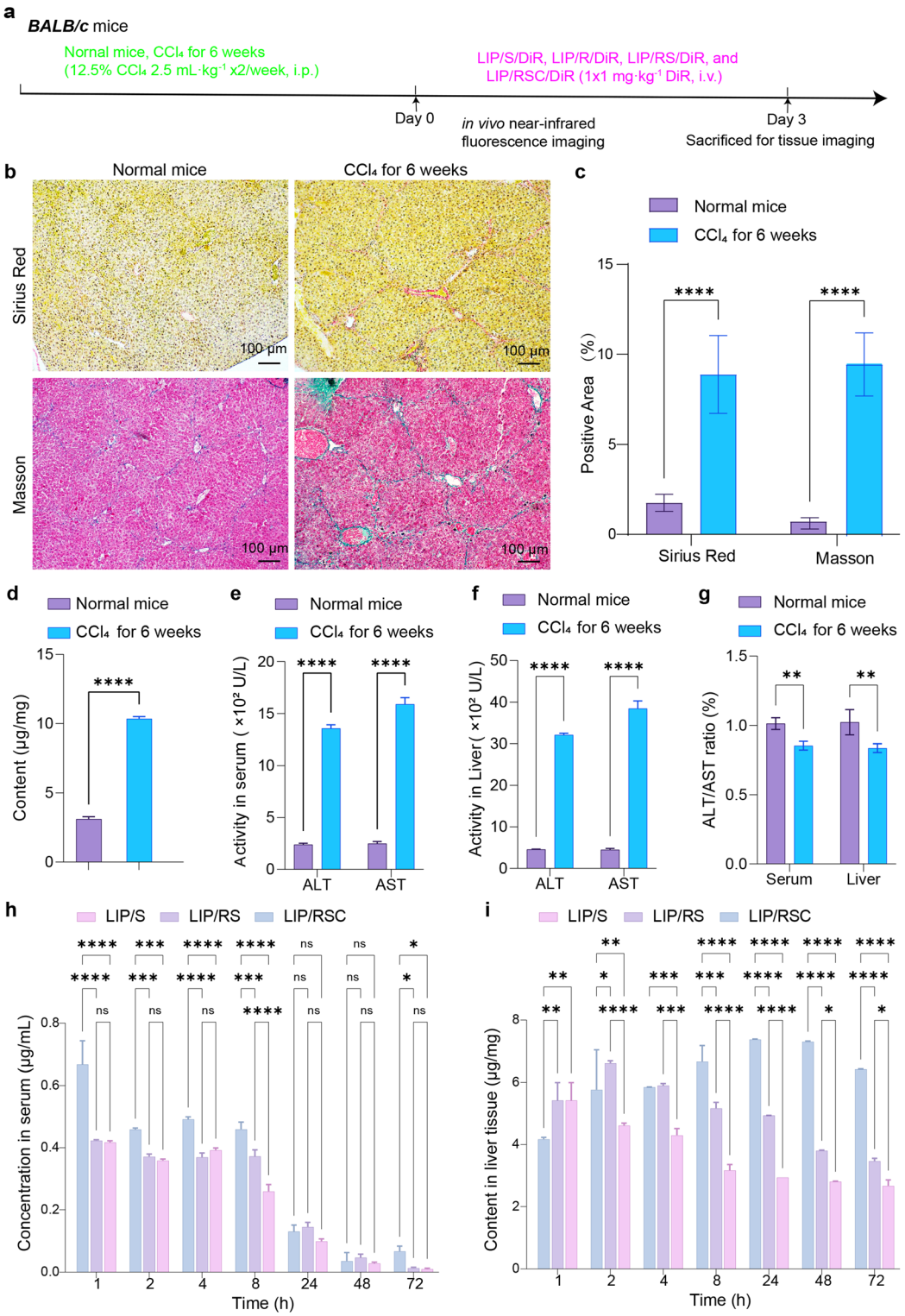

Fig. 6 Establishment of fibrotic mice models and metabolism of lipid nanomicelles *in vivo*. (a) Schematic summary of animal studies. (b) Representative Sirius Red and Masson's trichrome staining of liver sections from normal and treated mice. (c) Semi-quantitative analysis of the fibrotic area (percentage stained) from five sections using ImageJ software. (d). Total collagen in the liver quantified by biochemical assays. ALT and AST levels measured by biochemical assays ((e): serum; (f): liver; and (g): ALT/AST ratio). Pharmacokinetics of silybin-RA in LIP/S, LIP/RS and LIP/RSC *in vivo* ((h): serum and (i): liver). The data are expressed as the mean ± SD (n = 3). Error bars: *P < 0.05, **P < 0.01, ***P < 0.001, and ****P < 0.0001; "ns", no significant difference.

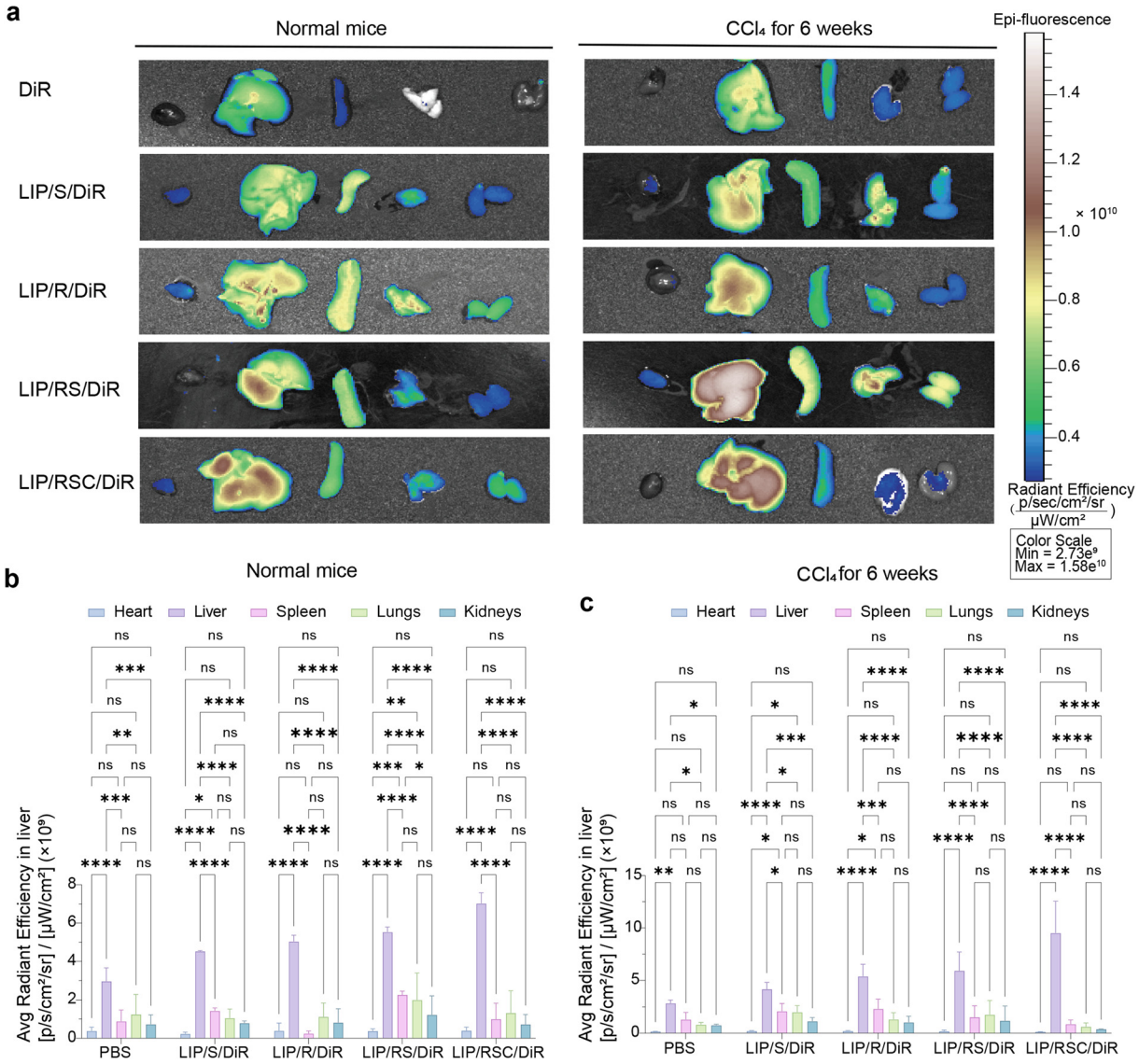

Fig. 7 Distribution of LIP nanomicelles in nonfibrotic and fibrotic mice. (a) Live imaging images of normal mice and model mice at day 3 after intravenous injection of different formulations (PBS, LIP/S, LIP/R, LIP/RS, LIP/RSC). (b) Statistical results of fluorescence intensity in the heart, liver, spleen, lungs, and kidneys of normal mice. (c) Statistical results of fluorescence intensity in the heart, liver, spleen, lungs, and kidneys of model mice. The data are expressed as the mean ± SD (n = 3). Error bars: *P < 0.05, **P < 0.01, ***P < 0.001, and ****P < 0.0001; "ns", no significant difference.

Consistent with our speculations, the biodistribution of liposomal micelles exhibited pathological-state dependency, with CCl_4-induced fibrotic mice demonstrating different hepatic metabolic capacities and fibrotic progressions compared to healthy controls. Fibrotic progression was manifested through three interconnected mechanisms: (i) deteriorating hepatic clearance function reducing micelle elimination; (ii) activated hepatic stellate cells enhancing micelle binding; and (iii) collagen accumulation impeding micelle permeation. Intra-fibrotic cohort heterogeneity in collagen deposition further influenced permeation variability, resulting in different peak accumulation times. Notably, LIP/RSC/DiR maintained superior hepatic accumulation in both healthy and fibrotic models.

The ideal liposome vectors require dual targeting specificity: preferential localization to activated HSCs beyond mere hepatotropism. To validate this paradigm, we loaded collagenase I/RA-modified liposomes (LIP/RSC) with 3,3′-dioctadecyloxacarbocyanine perchlorate (DiO), administering 3 successive daily intravenous doses to CCl_4 fibrotic mice. Terminal HSC analysis 24 h post-final injection combined α-SMA immunostaining (activated myofibroblast marker) with DAPI nuclear counterstaining. CLSM revealed predominant yellow colocalization signals (DiO: green; α-SMA: red) in LIP/RSC/DiO cohorts (Fig. 8). The therapeutic effects on liver fibrosis were further evidenced by a significant reduction in the α-SMA and hydroxyproline (Hyp) levels in the excised liver tissues of the LIP, LIP/S, LIP/R, LIP/RS, and LIP/RSC groups (SI Fig. S12), confirming ECM-penetrating

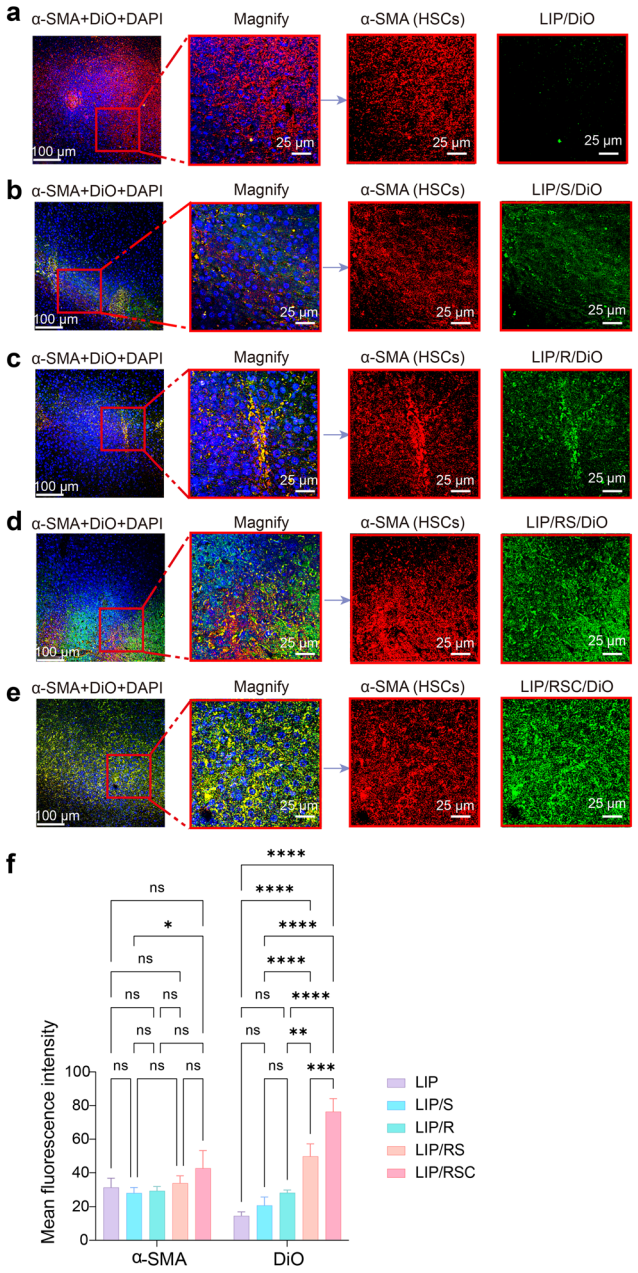

Fig. 8 Colocalization of DiO-labeled nanomicelles with activated HSCs in the livers of fibrotic mice. *In vivo* imaging and fluorescence aggregation at the liver site ((a): LIP; (b): LIP/S; (c): LIP/R; (d): LIP/RS; and (e): LIP/RSC). Liver tissue was sectioned and immunostained with an anti-α-SMA (smooth muscle actin) antibody (red) for activated HSCs and counterstained with a nuclear dye, DAPI (blue). Fluorescent DiO is shown in green. Colocalization was determined as yellow signals corresponding to perfect merges of green and red fluorescence. (f) Statistical results of fluorescence intensity using ImageJ software. Values are expressed as the mean ± SD (n = 3). Error bars: *P < 0.05, **P < 0.01, and ***P < 0.001; "ns", no significant difference.

vector competence mediated by enzymatic collagenolysis (collagenase I) and RA-guided HSC tropism. These multimodal targeting mechanisms synergistically enable fibrotic niche navigation and activated HSC precision delivery.

3.5 RA-targeted liposomal nanomicelles exhibit antifibrotic efficacy in murine liver fibrosis models

Serial intraperitoneal treatment of mice with CCl_4 three times per week for 6 weeks has been shown to cause nonlethal liver fibrosis as described above. By applying this fibrosis model to BALB/c mice, we further evaluated the effectiveness of administering liposomal micelle LIP/RSC on mouse fibrosis models. Therapeutic interventions involved administration three times weekly of four micellar formulations (LIP/S, LIP/R, LIP/RS, LIP/RSC) for 21 days, with terminal euthanasia performed 72 h post-final dose for comprehensive biochemical analysis (Fig. 9a). All treatment groups showed significant biomarker reduction, with LIP/RSC achieving near-normalization (Fig. 9b and c), demonstrating statistically comparable levels to healthy controls ($P > 0.05$).

Quantitative BioColor ECM analysis revealed pronounced collagen deposition differences: LIP/RSC treatment reduced collagen to 5.27 ± 0.63%, approaching physiological levels (Fig. 9d). Parallel patterns emerged for collagen subtypes (soluble: 9.51 ± 0.60% PBS *vs.* 1.90 ± 0.08% LIP/RSC; insoluble: 13.42 ± 0.54% PBS *vs.* 3.37 ± 0.10% LIP/RSC) (SI Fig. S13). This functional restoration reflects RA-mediated fibrotic targeting enabling collagenase I activation, which enhances silybin B/PPC synergy to inhibit early fibrogenesis, demonstrating the therapeutic efficacy of LIP/RSC against hepatic fibrosis.

Hepatic tissues were subjected to histopathological analysis *via* paraffin embedding and 3 μm sectioning, with subsequent Sirius Red, Masson's trichrome, and H&E staining (Fig. 9e). Quantitative morphometric analysis demonstrated significant fibrotic resolution: Masson's staining revealed a 9.1 ± 3.3% fibrotic area in PBS controls compared to the 1.7 ± 0.9% fibrotic area in LIP/RSC-treated specimens (normal: 0.77 ± 0.52%, Fig. 9f). Sirius Red quantification confirmed therapeutic efficacy gradients: 8.7 ± 2.7% (LIP/S), 6.7 ± 1.5% (LIP/R), and 2.8 ± 0.7% (LIP/RS) *versus* 0.63 ± 0.37% (LIP/RSC), with LIP/RSC restoring physiological collagen localization (perivascular distribution; PBS: 7.9 ± 2.6%; normal: 0.81 ± 0.28%; Fig. 9g). ELISA quantification revealed near-complete biomarker normalization under LIP/RSC treatment: Col I was reduced from 15.51 ± 0.76% (PBS) to 3.34 ± 0.47% (normal: 3.93 ± 0.07%, Fig. 9h) while TIMP1 decreased from 2.21 ± 0.13% to 0.94 ± 0.03% (normal: 0.92 ± 0.03%, Fig. 9i). Multi-organ histopathology (heart, spleen, lungs, kidneys) demonstrated treatment biosafety (SI Fig. S14). These data conclusively establish the dual therapeutic advantage of LIP/RSC: targeted collagen remodeling and systemic safety.

These integrated findings demonstrate that collagenase I modification enables liposomal nanomicelles (LIP/RSC) to traverse the fibrotic ECM barrier during systemic circulation, while RA modification confers specific HSC targeting. The synergistic co-modification results in enhanced delivery efficiency of LIP/RSC, manifested through preferential hepatic accumulation and precise HSC localization.

Hepatic fibrogenesis progressively reduces intercellular space through excessive collagen deposition, critically compro-

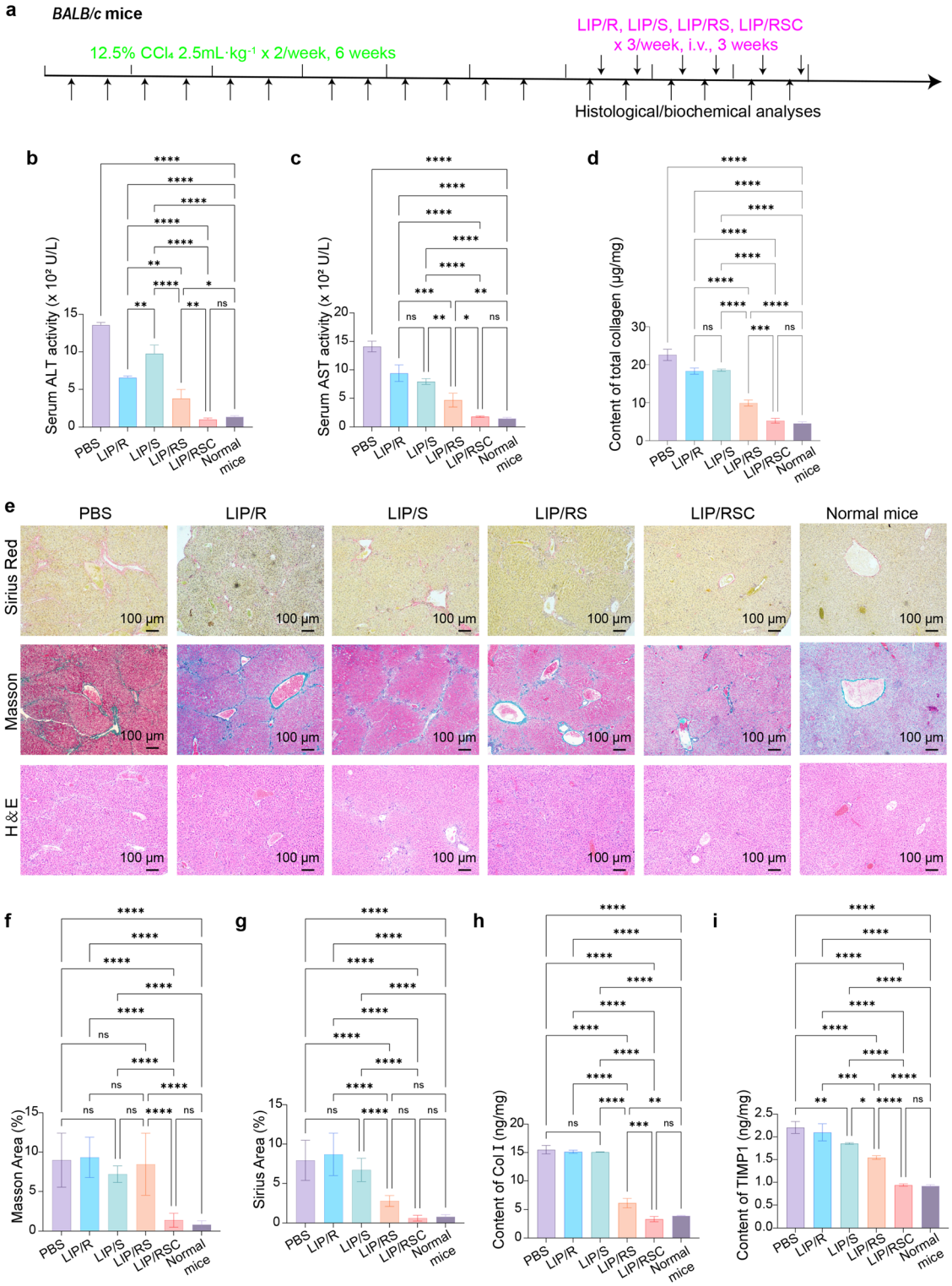

Fig. 9 Antifibrotic activity of LIP/RSC nanomicelles *in vivo*. (a) Schematic diagram showing the induction of hepatic fibrosis by CCl_4 in mice and administration of LIP/RSC micelles. (b and c) Serum ALT and AST levels measured by biochemical assays. (d) Quantitative analysis of total collagen by biochemical assays in the liver. (e) Representative liver sections stained with Sirius Red (collagen, red), Masson's trichrome (collagen, blue), and H&E (histopathology) staining. Semiquantitative analysis of the collagen deposition area from Masson's (f) and Sirius Red (g) staining (10 fields/section; n = 5 per mice). Col I (h) and TIMP1 (i) protein levels in liver homogenates. The data are expressed as the mean ± SD. Error bars: $^{*}P < 0.05$, $^{**}P < 0.01$, $^{***}P < 0.001$, and $^{****}P < 0.0001$; "ns", no significant difference.

mising the nanotherapeutic delivery to HSCs.[19,51,52] Our engineered cationic liposomal nanomicelle system (LIP/RSC) integrates RA-conjugated silybin B for targeted HSC delivery and hepatoprotective PPC for enhanced structural stability, demonstrating superior collagen barrier penetration and spatial specificity in fibrotic livers. The sequential drug liberation mechanism—combining lipid bilayer fusion at fibrotic lesions with pH-responsive hydrolytic activation in endolysosomal compartments (SI Fig. S15)—ensures the spatiotemporal control of therapeutic delivery, effectively minimizing off-target effects.

4. Conclusion

Therapeutic targeting of HSCs through nanodrug delivery systems faces significant challenges due to the pathological collagen accumulation in the space of Disse during hepatic fibrogenesis. This study presents a nano-scissors-structured liposomal micelle (LIP/RSC) exhibiting enhanced collagen barrier penetration in fibrotic livers and superior HSC-targeting efficiency.

Under collagen I-dominant barrier conditions, LIP/RSC achieved maximal cellular uptake through dual mechanisms: collagenase I-mediated proteolytic activity and retinol ligand-enhanced endocytosis. CLSM confirmed efficient intracellular payload release in LX-2 cells. Utilizing a non-lethal hepatic fibrosis model induced by CCl_4 intraperitoneal administration, we observed stage-dependent hepatic accumulation patterns of liposomal micelles. LIP/RSC exhibited good liver biodistribution following CCl_4 exposure for 6 weeks. Comparative immunofluorescence analysis revealed significantly improved drug delivery to activated HSCs by LIP/R (with RA, $P < 0.001$) and LIP/RSC (with RA and collagenase I, $P < 0.05$) *versus* LIP/S.

Silybin-RA induces redox imbalance by depleting GSH/GSSG ratios and increasing ROS levels (1.6-fold increase, $P < 0.0001$), triggering apoptosis in activated LX-2-CCl_4 cells through oxidative stress activation. Concurrently, collagenase I-functionalized LIP/RSC nanocarriers exhibit dual collagenolytic and rapid intracellular release properties, demonstrating enhanced penetration through Col I-rich fibrotic matrices ("nano-scissors" mechanism) for improved anti-fibrotic efficacy.

Therapeutic efficacy evaluation using silybin-RA-loaded LIP/RSC demonstrated superior anti-fibrotic activity in our chronic fibrosis model, achieving high hepatic bioavailability (83.2 ± 5.7%) and target specificity (HSC localization efficiency: 68.4 ± 6.3%). Comprehensive biocompatibility assessments confirmed excellent *in vitro* hemocompatibility (hemolysis < 5%) and cellular viability (>80% at 100 μM), with no observed acute/chronic toxicity in murine models (ALT/AST levels comparable to sham controls).

Multimodal validation through histomorphometric analysis, ECM quantification, and hepatic transaminase profiling (AST/ALT ratio reduction by 62.3%) established the therapeutic superiority of LIP/RSC. Key outcomes included ECM remodeling (collagen content reduction: 58.7 ± 4.2%, $P < 0.0001$ *vs.* PBS), especially Col I (content reduction: 78.5 ± 0.5%, $P < 0.0001$ *vs.* PBS), and TIMP1 normalization (1.32 ± 0.21 ng mL^{-1} *vs.* 3.84 ± 0.45 ng mL^{-1} in controls). Mechanistic studies revealed that collagenase I-modified nanovectors achieve therapeutic equilibrium through collagenolytic barrier modulation and sustained drug release kinetics.

This investigation establishes collagenase I functionalization as a paradigm-shifting strategy for overcoming fibrotic drug delivery barriers. LIP/RSC represents a promising next-generation therapeutic platform combining matrix-remodeling capability with precision HSC targeting, potentially transforming treatment paradigms for progressive hepatic fibrosis.

Author contributions

All authors agree with this publication. The study was done through contributions of all authors. Conceptualization: Yong Li, Yuanyuan Zhou, Lifang Wu and Wei Wang; data curation: Yuanyuan Zhou and Quanyuan Gao; formal analysis: Yong Li and Yuanyuan Zhou; investigation: Yuanyuan Zhou, Lifang Wu and Quanyuan Gao; methodology: Yong Li, Yuanyuan Zhou and Lifang Wu; validation: Yong Li, Yuanyuan Zhou and Wei Wang; visualization: Yuanyuan Zhou; writing – original draft preparation: Yong Li, Yuanyuan Zhou and Lifang Wu; writing – review and editing: Yong Li, Yuanyuan Zhou, Lifang Wu and Wei Wang; funding acquisition: Yong Li; project administration: Yong Li, Yuanyuan Zhou and Lifang Wu; resources: Yong Li, Yuanyuan Zhou, Lifang Wu and Quanyuan Gao; all authors have read and agreed to the published version of the manuscript.

Abbreviations

HSCs	Hepatic stellate cells
CCl_4	Carbon tetrachloride
ECM	Extracellular matrix
PDI	Polydispersity index
TEM	Transmission electron microscopy
DLS	Dynamic light scattering
FBS	Fetal bovine serum
WRL68 cells	Human hepatocyte cell line
LX-2 cells	Human hepatic stellate cell line
Cor6	Coumarin 6
Col I	Collagen I
DiR	1,1-Dioctadecyl-3,3,3′,3′-tetramethylindotricarbocyanine iodide
Cy3	Sulfo-cyanine3
DiO	3,3′-Dioctadecyloxacarbocyanine perchlorate
i.p.	Intraperitoneal injections
H&E	Hematoxylin and eosin
AST	Aspartate aminotransferase
ALT	Alanine aminotransferase

TIMP1	Tissue inhibitor of metalloproteinases-1
α-SMA	α-Smooth muscle actin
Hyp	Hydroxyproline

Conflicts of interest

The authors declare that they have no known competing financial interests or personal relationships that could have appeared to influence the work reported in this paper.

Data availability

The data will be made available from the corresponding author upon reasonable request.

Supplementary information (SI) is available. See DOI: https://doi.org/10.1039/d5bm01262g.

Acknowledgements

This work was supported by the General Program of the Fujian Natural Science Foundation (Grant No. 2024J011387) and we are grateful for the support of the Fujian Natural Science Foundation and Xiamen Medical Collage.

References

1 H. Devarbhavi, S. K. Asrani, J. P. Arab, Y. A. Nartey, E. Pose and P. S. Kamath, *J. Hepatol.*, 2023, **79**, 516–537.
2 X.-N. Wu, F. Xue, N. Zhang, W. Zhang, J.-J. Hou, Y. Lv, J.-X. Xiang and X.-F. Zhang, *BMC Public Health*, 2024, **24**, 363.
3 Z. Dong, Y. Wang and W. Jin, *MedComm*, 2024, **5**, e721.
4 A. J. Czaja, *Aliment. Pharmacol. Ther.*, 2014, **39**, 385–406.
5 D. Schuppan, M. Ashfaq-Khan, A. T. Yang and Y. O. Kim, *Matrix Biol.*, 2018, **68–69**, 435–451.
6 Y. A. Lee, M. C. Wallace and S. L. Friedman, *Gut*, 2015, **64**, 830–841.
7 A. Pellicoro, P. Ramachandran, J. P. Iredale and J. A. Fallowfield, *Nat. Rev. Immunol.*, 2014, **14**, 181–194.
8 R. G. Wells, *Gastroenterology*, 2009, **136**, 387–388.
9 K. Qu, T. Liu, T. Lin, X. Zhang, R. Cui, S. Liu, F. Meng, J. Zhang, M. Tai, Y. Wan and C. Liu, *Oncotarget*, 2016, **7**, 67650–67660.
10 G. Jesson, M. Brisander, P. Andersson, M. Demirbüker, H. Derand, H. Lennernäs and M. Malmsten, *Pharm. Res.*, 2014, **31**, 694–705.
11 T. Kisseleva and D. Brenner, *Nat. Rev. Gastroenterol. Hepatol.*, 2021, **18**, 151–166.
12 T. Tsuchida and S. L. Friedman, *Nat. Rev. Gastroenterol. Hepatol.*, 2017, **14**, 397–411.
13 C.-Y. Zhang, W.-G. Yuan, P. He, J.-H. Lei and C.-X. Wang, *World J. Gastroenterol.*, 2016, **22**, 10512–10522.
14 G. Ramadori, B. Saile, G. Ramadori and B. Saile, *Liver*, 2002, **22**, 283–294.
15 Y. Lee, J. Leslie, Y. Yang and L. Ding, *J. Exp. Med.*, 2020, **218**, e20200882.
16 K. Asahina, *J. Gastroenterol. Hepatol.*, 2012, **27**, 80–84.
17 L. Giannitrapani, M. Soresi, M. L. Bondì, G. Montalto and M. Cervello, *World J. Gastroenterol.*, 2014, **20**, 7242–7251.
18 L. H. Reddy and P. Couvreur, *J. Hepatol.*, 2011, **55**, 1461–1466.
19 L. F. Zhang, X. H. Wang, C. L. Zhang, J. Lee, B. W. Duan, L. Xing, L. Li, Y. K. Oh and H. L. Jiang, *ACS Nano*, 2022, **16**, 14029–14042.
20 Q.-Q. Fan, C.-L. Zhang, J.-B. Qiao, P.-F. Cui, L. Xing, Y.-K. Oh and H.-L. Jiang, *Biomaterials*, 2020, **230**, 119616.
21 W. H. Kong, K. Park, M.-Y. Lee, H. Lee, D. K. Sung and S. K. Hahn, *Biomaterials*, 2013, **34**, 542–551.
22 C. Jiménez Calvente, A. Sehgal, Y. Popov, Y. O. Kim, V. Zevallos, U. Sahin, M. Diken and D. Schuppan, *Hepatology*, 2015, **62**, 1285–1297.
23 L.-F. Zhang, W.-Q. Deng, Q.-W. Huang, J.-J. Zhang, Y. Wang, T.-J. Zhou, L. Xing and H.-L. Jiang, *Adv. Mater.*, 2024, **36**, 2311474.
24 B. Yu, S.-H. Hsu, C. Zhou, X. Wang, M. C. Terp, Y. Wu, L. Teng, Y. Mao, F. Wang, W. Xue, S. T. Jacob, K. Ghoshal, R. J. Lee and L. J. Lee, *Biomaterials*, 2012, **33**, 5924–5934.
25 X. Ruan, X. Cui, G. Jia, J. Wu, J. Zhao, D. J. Singh, Y. Liu, H. Zhang, L. Zhang and W. Zheng, *Chem. Eng. J.*, 2022, **428**, 132579.
26 E. C. Fuchs, R. Weyhenmeyer and O. H. Weiner, *Arzneimittelforschung*, 1997, **47**, 1383–1387.
27 G. Ramakrishnan, L. Lo Muzio, C. M. Elinos-Báez, S. Jagan, T. A. Augustine, S. Kamaraj, P. Anandakumar and T. Devaki, *Cell Proliferation*, 2009, **42**, 229–240.
28 G. Boigk, L. Stroedter, H. Herbst, J. Waldschmidt, E. O. Riecken and D. Schuppan, *Hepatology*, 1997, **26**, 643–649.
29 J. D. Jia, M. Bauer, J. J. Cho, M. Ruehl, S. Milani, G. Boigk, E. O. Riecken and D. Schuppan, *J. Hepatol.*, 2001, **35**, 392–398.
30 C. Loguercio, P. Andreone, C. Brisc, M. C. Brisc, E. Bugianesi, M. Chiaramonte, C. Cursaro, M. Danila, I. de Sio, A. Floreani, M. A. Freni, A. Grieco, M. Groppo, R. Lazzari, S. Lobello, E. Lorefice, M. Margotti, L. Miele, S. Milani, L. Okolicsanyi, G. Palasciano, P. Portincasa, P. Saltarelli, A. Smedile, F. Somalvico, A. Spadaro, I. Sporea, P. Sorrentino, R. Vecchione, C. Tuccillo, C. D. V. Blanco and A. Federico, *Free Radicals Biol. Med.*, 2012, **52**, 1658–1665.
31 L. F. Zhang, W. Q. Deng, X. H. Wang, Q. W. Huang, S. Q. Liang, Z. Q. Ding, L. Qi, Y. Wang, T. J. Zhou, L. Xing, J. W. Lee, Y. K. Oh and H. L. Jiang, *Adv. Sci.*, 2025, **12**, e2408898.
32 A. A. Ramadan, A. M. Elbakry, H. A. Sarhan and S. H. Ali, *Pharm. Dev. Technol.*, 2020, **25**, 1081–1089.
33 L. Wu, S. C. Chaudhary, V. R. Atigadda, O. V. Belyaeva, S. R. Harville, C. A. Elmets, D. D. Muccio, M. Athar and N. Y. Kedishvili, *PLoS One*, 2016, **11**, e0153556.

34 N. S. El-Mezayen, W. F. El-Hadidy, W. M. El-Refaie, T. I. Shalaby, M. M. Khattab and A. S. El-Khatib, *J. Controlled Release*, 2017, **266**, 226–237.
35 Y. T. Fan, T. J. Zhou, P. F. Cui, Y. J. He, X. Chang, L. Xing and H. L. Jiang, *Adv. Funct. Mater.*, 2019, **29**, DOI: 10.1002/adfm.201806708.
36 G. Onzi, S. S. Guterres, A. R. Pohlmann and L. A. Frank, in *The ADME Encyclopedia: A Comprehensive Guide on Biopharmacy and Pharmacokinetics*, Springer International Publishing, Cham, 2021, pp. 1–13, DOI: 10.1007/978-3-030-51519-5_108-1.
37 P. K. Mahalingaiah, R. Ciurlionis, K. R. Durbin, R. L. Yeager, B. K. Philip, B. Bawa, S. R. Mantena, B. P. Enright, M. J. Liguori and T. R. Van Vleet, *Pharmacol. Ther.*, 2019, **200**, 110–125.
38 Z. Chen, A. Jain, H. Liu, Z. Zhao and K. Cheng, *J. Pharmacol. Exp. Ther.*, 2019, **370**, 695–702.
39 L. Zhao, J. S. Son, B. Wang, Q. Tian, Y. Chen, X. Liu, J. M. de Avila, M.-J. Zhu and M. Du, *EBioMedicine*, 2020, **60**, 103020.
40 C. Liedtke, T. Luedde, T. Sauerbruch, D. Scholten, K. Streetz, F. Tacke, R. Tolba, C. Trautwein, J. Trebicka and R. Weiskirchen, *Fibrog. Tissue Repair*, 2013, **6**, 19.
41 N. Percie du Sert, V. Hurst, A. Ahluwalia, S. Alam, M. T. Avey, M. Baker, W. J. Browne, A. Clark, I. C. Cuthill, U. Dirnagl, M. Emerson, P. Garner, S. T. Holgate, D. W. Howells, N. A. Karp, S. E. Lazic, K. Lidster, C. J. MacCallum, M. Macleod, E. J. Pearl, O. H. Petersen, F. Rawle, P. Reynolds, K. Rooney, E. S. Sena, S. D. Silberberg, T. Steckler and H. Würbel, *PLoS Biol.*, 2020, **18**, e3000410.
42 Y. S. Lee and W. I. Jeong, *J. Gastroenterol. Hepatol.*, 2012, **27**(Suppl 2), 75–79.
43 Y. Sato, K. Murase, J. Kato, M. Kobune, T. Sato, Y. Kawano, R. Takimoto, K. Takada, K. Miyanishi, T. Matsunaga, T. Takayama and Y. Niitsu, *Nat. Biotechnol.*, 2008, **26**, 431–442.
44 Z. Zhang, C. Wang, Y. Zha, W. Hu, Z. Gao, Y. Zang, J. Chen, J. Zhang and L. Dong, *ACS Nano*, 2015, **9**, 2405–2419.
45 H. T. Duong, Z. Dong, L. Su, C. Boyer, J. George, T. P. Davis and J. Wang, *Small*, 2015, **11**, 2291–2304.
46 Q.-Q. Fan, C.-L. Zhang, J.-B. Qiao, P.-F. Cui, L. Xing, Y.-K. Oh and H.-L. Jiang, *Biomaterials*, 2020, **230**, 119616.
47 K. Hayashi, T. Maruhashi, W. Sakamoto and T. Yogo, *Adv. Funct. Mater.*, 2018, **28**, 1706332.
48 J.-B. Qiao, Q.-Q. Fan, L. Xing, P.-F. Cui, Y.-J. He, J.-C. Zhu, L. Wang, T. Pang, Y.-K. Oh, C. Zhang and H.-L. Jiang, *J. Controlled Release*, 2018, **283**, 113–125.
49 Z. Che, Z. Zhou, S.-Q. Li, L. Gao, J. Xiao and N.-K. Wong, *Trends Mol. Med.*, 2023, **29**, 951–967.
50 J.-L. Lu, C.-X. Yu and L.-J. Song, *Cell Death Discovery*, 2023, **9**, 449.
51 S. K. Meurer, M. A. Karsdal and R. Weiskirchen, *Expert Rev. Mol. Diagn.*, 2020, **20**, 947–969.
52 D. Sun, W. Gao, H. Hu and S. Zhou, *Acta Pharm. Sin. B*, 2022, **12**, 3049–3062.